



# Insight into the island-sea effect of Cu–N–C for enhanced CO<sub>2</sub> eletroreduction selectively towards C<sub>2</sub>H<sub>4</sub>

Haizhong Zhang<sup>a</sup>, Chao Zhu<sup>a</sup>, Renlan Liu<sup>b</sup>, Qile Fang<sup>c</sup>, Shuang Song<sup>a</sup>, Yi Shen<sup>a,\*</sup>

<sup>a</sup> Key Laboratory of Microbial Technology for Industrial Pollution Control of Zhejiang Province, College of Environment, Zhejiang University of Technology, Hangzhou 310032, PR China

<sup>b</sup> College of Life and Environmental Science, Wenzhou University, Wenzhou 325035, PR China

<sup>c</sup> Advanced Institute of Natural Sciences, Beijing Normal University at Zhuhai, Zhuhai 519087, PR China

## ARTICLE INFO

### Keywords:

Island-sea effect  
Single-atom and cluster catalyst  
Electrocatalysis  
Carbon dioxide reduction  
Ethylene

## ABSTRACT

The electrochemical reduction of CO<sub>2</sub> into C<sub>2</sub>H<sub>4</sub> with a high energy density and added value is a promising and desirable strategy for addressing carbon neutrality and energy shortage. However, the intricate peculiarity of the reaction limits the selectivity of atomically dispersed copper catalysts (ADCCs) towards C<sub>2</sub>H<sub>4</sub>, primarily due to the excessive number of electron transfer steps and the singular reactivity resulting from the presence of isolated single atoms or atom clusters. Herein, the Cu–N–C catalyst with a precisely controlled Island-sea structure (Island of atom cluster surrounded by the Sea with single atoms, namely Cu<sub>SA/AC</sub>–C<sub>3</sub>N<sub>4</sub>) delivered outstanding C<sub>2</sub>H<sub>4</sub> selectivity of up to 80.35 % (carbonaceous product ratio exceeding 99.4 %) and enhanced activity (a 56-fold increase in current density). Experimental and theoretical investigation further unveiled that the crucial intermediate \*CHO was generated at the Sea of single-atoms and then transferred to the Island of atom cluster with high reductive activity via the electron bridge, facilitating subsequent C–C coupling and deep reduction towards C<sub>2</sub>H<sub>4</sub>. Importantly, the Island-sea effect not only coupled the electron transfer processes but also facilitated the synergistic functionalization reactions involving the supply of \*H and C–C bond formation. This study provides novel insights and avenues for the development of enhanced M–N–C catalysts.

## 1. Introduction

The substantial anthropogenic emissions of CO<sub>2</sub> have contributed to environmental issues like the greenhouse effect and rising sea levels [1, 2]. To address this, the electrochemical reduction of CO<sub>2</sub> into chemical raw materials and energy has emerged as a promising and desirable strategy, albeit it poses considerable challenges [3–8]. Recently, remarkable progress has been achieved in the electrochemical reduction of CO<sub>2</sub> to C<sub>1</sub> products, including CO and HCOOH, using catalysts based on noble metals (e.g., Au and Ag) and transition metal single-atom catalysts (e.g., M–N–C, where M = Ni, Fe, Co, etc.) [9–12]. Nevertheless, achieving efficient and selective deep reduction of CO<sub>2</sub> into high-energy density and value-added C<sub>2</sub> products, such as C<sub>2</sub>H<sub>4</sub>, continues to pose a substantial challenge. This is attributed to the more demanding catalytic process involving the 12-electron transfer and intricate C–C coupling steps compared to the reduction of CO<sub>2</sub> to C<sub>1</sub> products [13]. Therefore, it is worthwhile to further investigate the design of a feasible electrocatalyst for CO<sub>2</sub> reduction reaction (CO<sub>2</sub>RR)

that specifically aims to produce C<sub>2</sub>H<sub>4</sub>.

To date, it has been demonstrated that the process of CO<sub>2</sub>→C<sub>2</sub>H<sub>4</sub> involves the reduction from CO<sub>2</sub> to C<sub>1</sub> intermediates, C–C coupling, and the subsequent reduction to C<sub>2</sub>H<sub>4</sub> [14–17]. The abundance of C<sub>1</sub> species is beneficial for the dimerization reaction of the pivotal intermediate \*C<sub>1</sub>, which is considered the rate-determining step in the CO<sub>2</sub>→C<sub>2</sub>H<sub>4</sub> pathway [18,19]. Copper (Cu), as a primary metal for the deep reduction of CO<sub>2</sub>, exhibits the ability to selectively convert CO<sub>2</sub> into C<sub>2</sub>H<sub>4</sub> [20–24]. Among them, the significant specific surface area, elevated metal surface free energy, and exceptionally high electron activity of atomically dispersed Cu catalysts (ADCCs, including Cu single-atom catalysts and atom cluster catalysts) brought excellent adsorption performance and reactivity, making it effective against CO<sub>2</sub>RR [25,26]. However, it is precisely because of the aforementioned properties that ADCCs might convert CO<sub>2</sub> to a variety of products such as CO, CH<sub>4</sub>, HCOOH, etc., resulting in diminished selectivity and constraining their practical implementation [27–30]. Furthermore, due to the complexity of the CO<sub>2</sub>→C<sub>2</sub>H<sub>4</sub> reaction, the single active sites of ADCCs are quite

\* Corresponding author.

E-mail address: [shenyi@zjut.edu.cn](mailto:shenyi@zjut.edu.cn) (Y. Shen).

<https://doi.org/10.1016/j.apcatb.2023.123566>

Received 26 October 2023; Received in revised form 18 November 2023; Accepted 25 November 2023

Available online 28 November 2023

0926-3373/© 2023 Elsevier B.V. All rights reserved.

challenging for the C–C coupling step and therefore do not exhibit high  $C_2H_4$  activity and selectivity. Various strategies have been developed to enhance the activity and selectivity of ADCCs towards  $C_2$  products, including modulation of oxidation states [31–34], doping with heteroatoms [35–37], and modification of foreign molecules. Despite these efforts, achieving high activity and selectivity for direct  $CO_2$  reduction to  $C_2H_4$  remains a formidable challenge. Because isolated and individual single atoms or atom clusters are unable to accommodate excessive electron transfer steps, as well as to effectively simultaneously fulfill protonation, coupling, and supply of  $C_1$  intermediate. It is imperative to explore innovative approaches in the design of atomic-scale copper-based catalysts to achieve efficient  $CO_2$  reduction to  $C_2H_4$ .

Recently, the wide range application of catalysts with atom clusters and functionalized single-atom metal has been demonstrated in the field of catalysis. For instance, the Co single atoms actively surround PtCo alloy nanoparticles, forming a dual-site integrated system capable of simultaneously producing  $H_2$  and  $O_2$  with high efficiency [38]. The presence of Au (111) clusters in the catalyst modulates the d-band structure of Pt single atoms, promoting the performance of Pt single atoms in the multi-step deep oxidation reactions of methanol and ethanol [39]. Therefore, the construction of efficient and robust "cluster-single atom" systems with specific dual-active sites for the targeted reaction holds promise for developing novel atomic catalysts with high activity and selectivity [40,41]. In these systems, one site generates  $C_1$  species that are subsequently converted to  $C_2H_4$  by an adjacent site, which simultaneously achieved the concatenation of multiple electron transfer steps and the collaboration of different reaction functions, offering potential solutions to the challenges associated with ADCCs in  $CO_2$  to  $C_2H_4$  conversion [9]. However, the precise control and methods at the atomic scale for this structure, as well as a comprehensive understanding of the enhancement mechanism of active sites in  $CO_2$ RR, are still lacking. This paradigm is still in its early stages and necessitates prompt advancements.

Herein, a Cu–N–C catalyst with an Island-sea structure ( $Cu_{SA}/AC-C_3N_4$ ) was designed by precisely controlling the dispersion of Cu single atoms and atom clusters. The distribution and fine electronic structure of the Island-sea structure have been determined using high-angle annular dark-field scanning transmission electron microscopy (HAADF-STEM) and extended X-ray absorption fine structure (EXAFS) analysis. To the best of our knowledge, it surpasses the majority of reported literature, delivering outstanding  $C_2H_4$  selectivity of up to 80.35 % (a carbonaceous product ratio exceeding 99.4 %) and a 56-fold increase in current density. Density functional theory (DFT) and in-situ surface-enhanced Raman spectroscopy (SERS) provided further insight into the Island-sea effect with three key steps of the  $C_2H_4$  formation, that the generation of  $^*CHO$  at the Sea with single atoms, the C–C coupling on the Island of atom cluster, and the migration of  $^*CHO$  from the Sea to the Island via the electron bridge between them. The complex multi-electron steps and single-function of individual sites were collectively integrated through the Island-sea, which significantly sped up the formation of  $C_2H_4$ . This study provides a new strategy and valuable insights for addressing the challenges associated with the electrocatalytic reduction of  $CO_2$  to  $C_2H_4$  and the development of innovative atomic catalysts.

## 2. Experimental section

### 2.1. Synthesis of catalysts

#### 2.1.1. Synthesis of g- $C_3N_4$

5 g of melamine powder was placed to an alumina crucible (100 mL). Subsequently, the crucible was sealed with crucible lid and multiple layers of tin foil and put into a muffle furnace with the heating program from 25 °C to 550 °C at the rate of 2.5 °C min<sup>−1</sup> and the retention time at 550 °C was 3 h. Finally, the yellowish-white solid obtained by above operation was ground with an onyx mortar to get yellow g- $C_3N_4$  powder.

#### 2.1.2. Synthesis of Cu–N/O complex

Solution B and solution C was added to solution A and the mixed solution was stirred for 1 h. Centrifuging to obtain the solid substance and wash it three times with water and methanol respectively. Finally, the light blue solid was obtained by drying in vacuum. The detailed preparation process of solution A, B, and C was as follows: Solution A: 2.0 mmol 341 mg  $CuCl_2 \cdot 2H_2O$  was ultrasonically dispersed in 20 mL deionized water; Solution B: 0.3 mmol 46.5 mg 2,2-bipyridine was ultrasonically dispersed in 10 mL methanol; Solution C: 1.8 mmol 225 mg oxalic acid was ultrasonically dispersed in 10 mL deionized water.

#### 2.1.3. Synthesis of Cu– $C_3N_4$

Solution A: 27.6 mg  $CuCl_2 \cdot 2H_2O$  was ultrasonically dispersed in 55 mL deionized water. Adding 0.5 g g- $C_3N_4$  to solution A and kept stirring for 24 h. The resulting solid matter was maintained at 400 °C under an inert gas atmosphere for 2 h (the rate of 2 °C min<sup>−1</sup>). Finally, a yellow solid was obtained.

Detailed methods are provided in the SI.

### 2.2. $CO_2$ reduction reaction measurements

Electrochemical studies were carried out in electrochemical flow diffusion cell, which including gas chambers, cathode chambers, and anode chambers. The anodic and cathodic chambers were separated by an ion exchange membrane (Fumasep FAA-3-PK-130). Catalyst inks were air-brushed onto carbon paper (1 cm × 3 cm) with a mass loading of  $\sim 0.3$  mg cm<sup>−2</sup> served as the cathode electrodes (working electrode). Ag/AgCl electrode (saturated KCl) and Ni foam were used as the reference electrode and anode electrodes, respectively. The electrolysis was conducted using CORRTTEST Bi-potentiostat. Detailed methods are provided in the SI.

### 2.3. Characterization

Powder X-ray diffraction (XRD) measurements were performed on a SmartLab SE diffractometer using Cu targets (tube voltage: 40 kV, current: 30 mA). The functional group structure was measured by Fourier transform infrared spectroscopy (FT-IR). ICP-OES results were obtained by assays from Agilent 5110 instruments. The morphology of samples was observed through a field emission scanning electron microscope (FE-SEM, HITACHI Regulus 8100) at an acceleration voltage of 15 kV. Sample topography was also observed using transmission electron microscopy (TEM, FEI, Tecnai G2 F30), and atomic-resolution HAADF-STEM was performed using a state-of-the-art transmission electron microscope equipped with double (image and probe) spherical aberration (Cs) correctors (Thermo Scientific Spectra 300). The total specific surface area of the material was obtained by the Brunauer Emmett Teller method (BET). At a vacuum of 300 °C, the sample was pretreated for 24 h using the Micro instrument Standard Degassing Station. Then the sample was subjected to nitrogen aspiration and desorption testing using a 4-stop automatic specific surface area analyzer of the American Micromeritics APSP2460 model under 77 k liquid nitrogen conditions. After the instrument analysis was completed, the isothermal suction and desorption curve was obtained.

X-ray photoelectron spectroscopy (XPS) spectra were collected with an ESCALAB 250Xi instrument using an Al K $\alpha$  X-ray as an excitation source. Both the Ni K-edge and Cu K-edge spectra were recorded under fluorescence mode at the BL14W beamline in the Shanghai Synchrotron Radiation Facility (SSRF).

### 2.4. Computation framework

In Density Functional Theory calculations, slab model of  $Cu_{SA}-C_3N_4$ ,  $Cu_{SA}/AC-C_3N_4$ ,  $Cu_{AC}-C_3N_4$  were built. Structural optimization was performed by Vienna Ab-initio Simulation Package (VASP) [42] with the projector augmented wave (PAW) method [43]. The

exchange-functional was treated using the Perdew-Burke-Ernzerhof (PBE) [44] functional, in combination with the DFT-D3 correction [45]. The cut-off energy of the plane-wave basis was set at 450 eV in structural optimization. For the optimization of both geometry and lattice size, the Brillouin zone integration was performed with a Monkhorst-pack [46] k-point mesh of  $3 \times 3 \times 1$ . The self-consistent calculations applied a convergence energy threshold of  $10^{-5}$  eV. The equilibrium geometries and lattice constants were optimized with maximum stress on each atom within  $0.02 \text{ eV } \text{\AA}^{-1}$ . Spin polarization method was adopted to describe magnetism brought by slab model. Isosurface level of charge density difference of  $\text{Cu}_{\text{SA}}-\text{C}_3\text{N}_4$ ,  $\text{Cu}_{\text{SA/AC}}-\text{C}_3\text{N}_4$  and  $\text{Cu}_{\text{AC}}-\text{C}_3\text{N}_4$  was set at  $0.01 \text{ e } \text{\AA}^{-3}$ . Density of states of  $\text{Cu}_{\text{SA/AC}}-\text{C}_3\text{N}_4$  and  $\text{Cu}_{\text{SA/AC}}-\text{C}_3\text{N}_4-\text{CHO}-\text{CO}$  were both obtained by vaspkit interface [47]. Detailed methods are provided in the SI.

### 3. Results and discussion

#### 3.1. Characteristic of $\text{Cu}_{\text{SA/AC}}-\text{C}_3\text{N}_4$

To prepare catalysts with both single-atom and atom cluster sites, it is customary to employ an excess of metal precursors to take advantage of the high overlap between adsorption sites and coordination sites, inducing aggregation of atoms and formation of atom clusters. However,

this process is often random and uncontrollable, making it difficult to achieve uniformly dispersed sites of atom clusters and single atoms in the synthesized catalyst structure. Hence, we employed a strategy of chelating copper atoms with ligands in a certain ratio followed by selectively removing low-thermally stable ligands, which facilitated the migration and aggregation of Cu atoms into well-defined clusters, enabling precise modulation of highly dispersed Cu single-atom and atom cluster sites. In this process, the atom cluster sites were separated into "Islands" by the single atom sites, ultimately forming the Island-sea structure of  $\text{Cu}_{\text{SA/AC}}-\text{C}_3\text{N}_4$  as illustrated in Fig. 1a. Firstly,  $\text{Cu}^{2+}$  was captured with oxalic acid, followed by formed Cu–N/O complexes [48] with highly dispersed Cu by chelation with 2,2'-bipyridine. These complexes were then self-assembled onto g- $\text{C}_3\text{N}_4$  support and were subsequently pyrolyzed to remove oxalic acid for migrating and agglomerating Cu atoms into clusters. Then, it experienced calcination at  $400^\circ\text{C}$  under inert ambient to obtain  $\text{Cu}_{\text{SA/AC}}-\text{C}_3\text{N}_4$ . Due to the 2, 2'-bipyridine ligands dispersed and immobilized Cu atoms well through coordinate covalent bonds, they effectively prevented the migration and agglomeration of Cu single atoms during calcination. Upon removal of the 2,2'-bipyridine ligands during calcination, the anchoring of Cu single atoms onto the g- $\text{C}_3\text{N}_4$  support was successfully accomplished. Specifically, both ligands can effectively disperse and anchor Cu. Upon removal of the low thermal stability ligand, Cu becomes less stable,

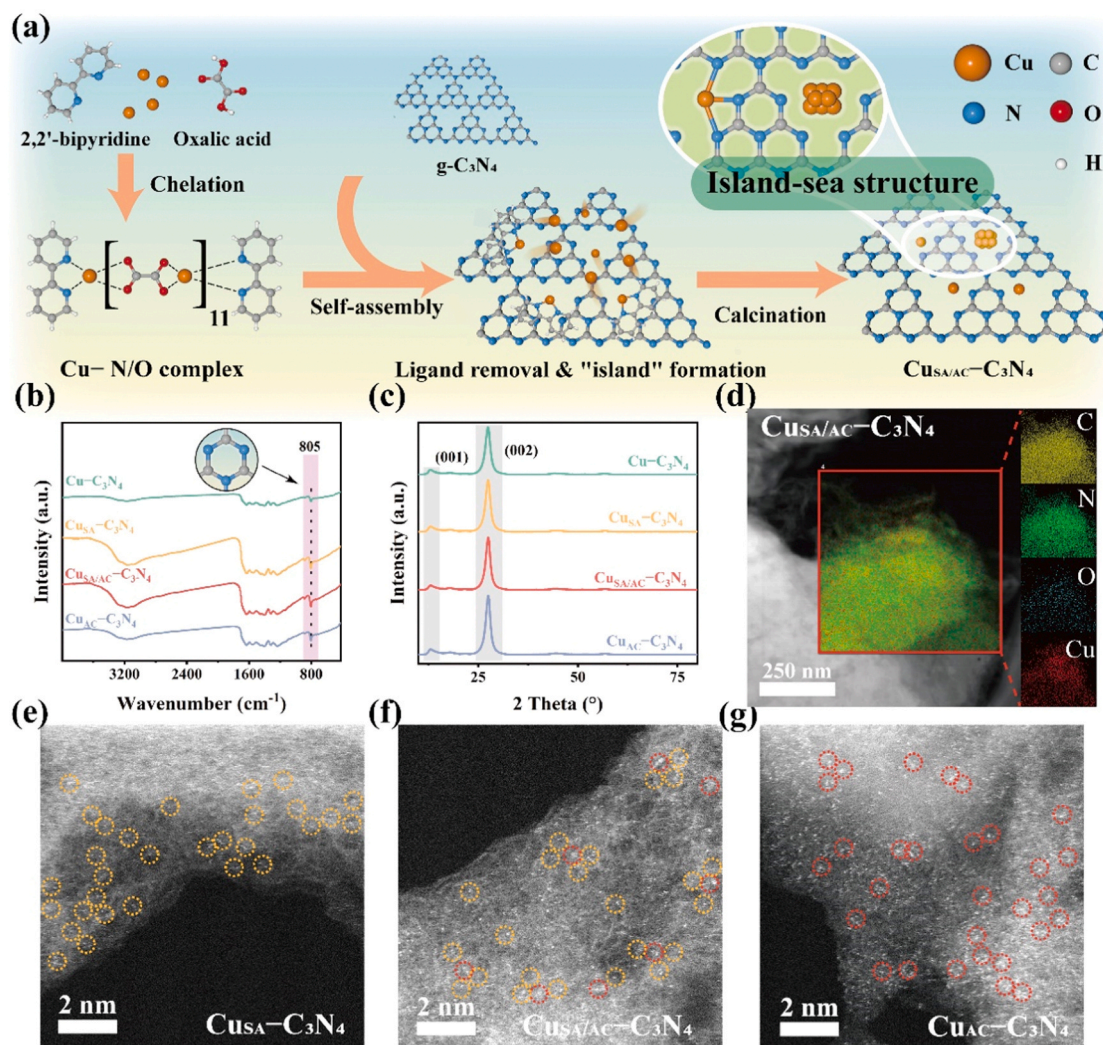


**Fig. 1.** (a) Schematic diagram of the synthesis of  $\text{Cu}_{\text{SA/AC}}-\text{C}_3\text{N}_4$ . (b) FT-IR spectra, and (c) XRD pattern of  $\text{Cu}-\text{C}_3\text{N}_4$ ,  $\text{Cu}_{\text{SA}}-\text{C}_3\text{N}_4$ ,  $\text{Cu}_{\text{SA/AC}}-\text{C}_3\text{N}_4$  and  $\text{Cu}_{\text{AC}}-\text{C}_3\text{N}_4$ . (d) HR-TEM and corresponding EDX mapping images of  $\text{Cu}_{\text{SA/AC}}-\text{C}_3\text{N}_4$ . Spherical aberration-corrected HAADF-STEM image corrected for (e)  $\text{Cu}_{\text{SA}}-\text{C}_3\text{N}_4$ , (f)  $\text{Cu}_{\text{SA/AC}}-\text{C}_3\text{N}_4$  and (g)  $\text{Cu}_{\text{AC}}-\text{C}_3\text{N}_4$  marked with circles.



migrating and aggregating into clusters at elevated temperatures. The high thermal stability ligand serves as a cleavage point, preventing excessive aggregation of Cu to form the nanoparticles. Therefore, if the oxalic acid was removed (pre-removal step) before anchoring the Cu atoms by calcination, the partial Cu atoms would lose the ligand stabilization and dissipate absorbed energy, facilitating their translocation and amalgamation, thereby exerting control over the formation of the Cu clusters. Eventually, the single-atom sites and cluster sites of Cu atoms culminated in the formation of the Island-sea structure. For comparison and exploration, control samples containing Cu single atoms ( $\text{Cu}-\text{C}_3\text{N}_4$  and  $\text{Cu}_{\text{SA}}-\text{C}_3\text{N}_4$ ) were prepared using equal amounts of Cu in the conventional impregnation method and the method mentioned above without the ligand pre-removal step, respectively. Additionally, a Cu atom cluster sample ( $\text{Cu}_{\text{AC}}-\text{C}_3\text{N}_4$ ) which underwent complete removal of ligands before calcination, was also prepared to facilitate further analysis and comparison.

The successful synthesis of  $\text{g}-\text{C}_3\text{N}_4$  was confirmed through FT-IR. In Fig. 1b, all samples exhibited characteristic peaks, including the breath mode of the tri-s-triazine units at  $810\text{ cm}^{-1}$ , the C–N heterocyclic stretching vibration in the range of  $1200\text{--}1650\text{ cm}^{-1}$ , and the wide stretching vibration pattern of the –NH group around  $3200\text{ cm}^{-1}$  [49]. However, the characteristic peak of  $\text{g}-\text{C}_3\text{N}_4$  in the  $\text{Cu}-\text{C}_3\text{N}_4$  sample was notably weaker compared to the other samples, indicating that the presence of ligands could ensure the integrity of the interlamellar structure of the  $\text{g}-\text{C}_3\text{N}_4$  and prevent the destruction of C–N heterocycles due to long-term impregnation. Additionally, in the Cu–N/O complexes (Fig. S1), oxalic acid-associated hydroxyl (O–H) stretching characteristic peaks ( $3450\text{ cm}^{-2}$ ) were not observed, proving the successful coordination of  $\text{Cu}^{2+}$  with the  $\text{O}^{-1}$  of hydroxyl. Correspondingly, in  $\text{Cu}_{\text{SA}}-\text{C}_3\text{N}_4$ , carbonyl (C=O) stretching features (around  $1670\text{ cm}^{-1}$ ) associated with oxalic acid were not observed and the redshift of the pyridine N-associated characteristic peaks, substantiating complete removal of ligands during immobilization of Cu [50]. Moreover, the results of inductively coupled plasma-mass spectrometry (ICP-MS) confirmed the successful loading of Cu in all samples, with a Cu content of 0.46 % in  $\text{Cu}_{\text{SA}/\text{AC}}-\text{C}_3\text{N}_4$  (Table S1). The XRD data (Fig. 1c) showed diffraction peaks matching the repeated tri-s-triazine structure (001) and the accumulation of the carbon nitride  $\pi$  conjugate plane of the graphite phase (002), proving that the loading of Cu did not alter the crystal structure of  $\text{g}-\text{C}_3\text{N}_4$  [51]. All catalysts present a characteristic diffraction pattern of the  $\text{g}-\text{C}_3\text{N}_4$  without any impurities. More importantly, there was no peak from crystalline metal oxides or metal nanoparticles, hence, it can be deduced that Cu existed in the form of single atoms or atom clusters.

Subsequently, the morphology of the samples was examined using electron microscopy. The SEM images (Fig. S2a) revealed that the Cu–N/O complexes appeared as fragmented smooth lumps, which differed significantly from the typical layered structure of  $\text{g}-\text{C}_3\text{N}_4$  shown in Fig. S2b. As depicted in Fig. S2c–f, the layered structure of the original  $\text{g}-\text{C}_3\text{N}_4$  was well preserved in all samples, but the sizes gradually decreased with increasing pyrolysis time and loading of Cu. It can be observed that the elements were evenly distributed, as shown in Fig. S3. The absence of the Cu–N/O complexes in all samples further proves the removal of ligands during Cu fixation and ensured the purity of these catalysts. The HR-TEM was employed to further observe the structure and elemental distribution of the catalysts (Fig. S4). Numerous nanoscale pores were observed in  $\text{Cu}-\text{C}_3\text{N}_4$ , marked within blue circles, which may be caused by prolonged impregnation of metal salt solutions. It supported the previous analysis that the strategy of ligand chelating Cu atoms could improve the impact of metal loading processes on substrate structure. In the EDX image of  $\text{Cu}_{\text{SA}}-\text{C}_3\text{N}_4$  (Fig. S5), the C, N, O, and Cu elements were evenly distributed with a lower distribution of Cu. However, a large number of densely distributed Cu was observed in the counterpart image of  $\text{Cu}_{\text{SA}/\text{AC}}-\text{C}_3\text{N}_4$  (Fig. 1d). This region was further transferred to bright-field and continuously zoomed in (Fig. S6), and no crystal lattice image belonging to nanoparticles was detected. Therefore,

the strong Cu signal may be attributed to a high density of Cu single atoms or atom clusters, providing further evidence for the Island-sea structure including Cu single atoms and clusters would be present.

The spherical aberration-corrected HAADF-STEM further revealed the detailed Cu atomic structure in the catalysts. As shown in Fig. 1e and Fig. S7, a higher abundance of single atom sites was distributed in  $\text{Cu}_{\text{SA}}-\text{C}_3\text{N}_4$  compared to in  $\text{Cu}-\text{C}_3\text{N}_4$ , all of which were enclosed by orange circles. The increase of single-atom sites in  $\text{Cu}_{\text{SA}}-\text{C}_3\text{N}_4$  once again demonstrated that the preparation of single-atom catalysts using Cu–N/O complexes could effectively enhance the loading and dispersion of Cu species. Satisfactorily, distinct sites with a brighter and larger appearance than in  $\text{Cu}-\text{C}_3\text{N}_4$  and  $\text{Cu}_{\text{SA}}-\text{C}_3\text{N}_4$  were clearly observed in  $\text{Cu}_{\text{SA}/\text{AC}}-\text{C}_3\text{N}_4$  and  $\text{Cu}_{\text{AC}}-\text{C}_3\text{N}_4$  (Fig. 1f,g), identified by red circles. These sites may be atom clusters consisting of several atoms formed by migration and agglomeration of Cu atoms due to the early removal of ligands and heating [52]. Moreover, in contrast to  $\text{Cu}_{\text{AC}}-\text{C}_3\text{N}_4$  with a mass of denser atom cluster sites, there were a handful atom clusters observed in  $\text{Cu}_{\text{SA}/\text{AC}}-\text{C}_3\text{N}_4$ , which were separated and surrounded by Cu single atoms to form the Island-sea structures as annotated in Fig. 1a. The size of Cu clusters and site distance in different catalysts were statistically analyzed to confirm information of site structure. The size distribution of Cu clusters was relatively concentrated, mainly around 0.25 nm (Fig. S8). The statistical results of site distance between different catalysts were shown in Figs. S9–S11. The atomic distance in  $\text{Cu}_{\text{SA}}-\text{C}_3\text{N}_4$  was concentrated at about 0.55 nm, the distance between Cu clusters in  $\text{Cu}_{\text{AC}}-\text{C}_3\text{N}_4$  was basically above 0.5 nm, and the distance between single atoms and clusters in  $\text{Cu}_{\text{SA}/\text{AC}}-\text{C}_3\text{N}_4$  was mostly 0.35 nm. The relatively close distance between the "island" of Cu clusters and the "sea" of Cu single atoms set the stage for synergy.

To reveal the effects of Cu species on the adsorption performance and active site characteristics of the catalyst, the porous structure of the catalyst was further analyzed (Figs. S12, S13, and Table S2). The  $\text{N}_2$  adsorption-desorption curve of the H3 type suggested the presence of rich mesopores and the conformity to the layered structure of  $\text{g}-\text{C}_3\text{N}_4$ , which was consistent with the results observed under electron microscopy previously. Furthermore, the Brunauer Emmett Teller (BET) specific surface area of  $\text{Cu}_{\text{SA}/\text{AC}}-\text{C}_3\text{N}_4$  exceeded that of all other catalysts. Especially,  $\text{Cu}_{\text{SA}/\text{AC}}-\text{C}_3\text{N}_4$  exhibited the smallest microporous surface area other than  $\text{Cu}-\text{C}_3\text{N}_4$  and the highest microporous volume, resulting in the largest average size of micropores. The obvious difference in the volume and surface area of micropores of different catalysts indicated a close relationship between the active sites and micropore formation. It was anticipated that these micropores would enhance the density and exposure of active sites, further facilitate electrolyte penetration and thereby improve the overall catalytic activity of  $\text{Cu}_{\text{SA}/\text{AC}}-\text{C}_3\text{N}_4$  [53,54].

The surface elemental composition and associated electronic properties of the catalysts were determined by X-ray photoelectron spectroscopy (XPS), as shown in Fig. 2, Figs. S14–S17, and Table S3. The peaks at  $\sim 398$ ,  $\sim 399$ ,  $\sim 401$ , and  $\sim 404\text{ eV}$  in the N 1s spectrum related to C–N = C, Cu–N, –NH, and  $\pi-\pi^*$  conjugation of carbon nitride graphite phase, respectively (Fig. 2a) [55,56]. The presence of the Cu–N peak demonstrated that Cu predominantly bonded to N atoms on  $\text{g}-\text{C}_3\text{N}_4$  [57–62]. Besides, compared to samples prepared by the Cu–N/O complexes method, the N 1s binding energy in  $\text{Cu}-\text{C}_3\text{N}_4$  showed an overall trend towards low energy, indicating that the former had a stronger electron affinity, thus providing a more stable coordination environment and better adsorption capability. In this coordination environment, electron transfer from N atoms to Cu atoms in Cu–N units obviously increased. The decrease in the binding energy of Cu–N peak of  $\text{Cu}_{\text{SA}/\text{AC}}-\text{C}_3\text{N}_4$  and  $\text{Cu}_{\text{AC}}-\text{C}_3\text{N}_4$  stemmed from the presence of atom clusters promoting the transfer of some electrons in Cu–N to Cu–Cu. And the increase in their Cu–N content was more than 50 % ascribing from the decrease of ligands before calcination, which increased the number of Cu single atom sites. Crucially, the slight difference in Cu–N content between  $\text{Cu}_{\text{SA}/\text{AC}}-\text{C}_3\text{N}_4$  and  $\text{Cu}_{\text{AC}}-\text{C}_3\text{N}_4$  suggested that the increase of Cu loading, as determined by ICP-MS, was mainly attributed to

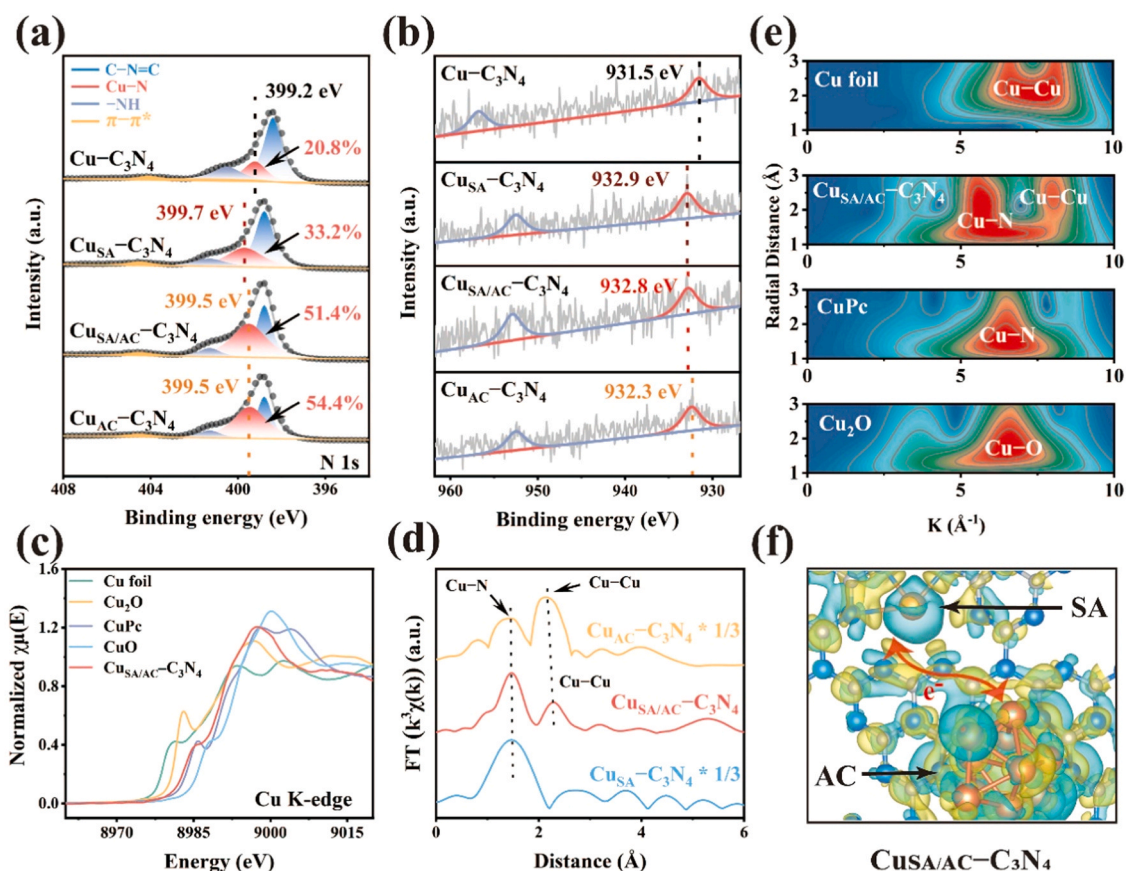


**Fig. 2.** (a) High-resolution N 1s spectra. (b) High-resolution Cu 2p spectra. (c) Cu K-edge XANES spectra of the samples. (d) Cu K-edge FT-EXAFS curves of the samples. (e) WT plots of Cu foil, CuSA/AC-C<sub>3</sub>N<sub>4</sub>, CuPc, and Cu<sub>2</sub>O. (f) The charge density difference distribution of CuSA/AC-C<sub>3</sub>N<sub>4</sub>.

the increased atom clusters. In Cu 2p core-level XPS spectra (Fig. 2b), the Cu 2p<sup>3/2</sup> peaks of CuSA-C<sub>3</sub>N<sub>4</sub> at ~932.9 eV revealed that the valence state of the Cu single atoms was between +1 (932.3 eV) and +2 (935.0 eV) [63]. Analogously, in CuSA/AC-C<sub>3</sub>N<sub>4</sub> and CuAC-C<sub>3</sub>N<sub>4</sub>, the Cu 2p<sup>3/2</sup> peak moved towards low binding energy, indicating increased electron transfer from N atoms to Cu atoms in Cu-N, which was due to charge redistribution in the aggregation of non-N-coordinated Cu in atom clusters. The shift in binding energy of Cu in CuSA/AC-C<sub>3</sub>N<sub>4</sub> and CuAC-C<sub>3</sub>N<sub>4</sub> revealed a decrease in the average valence state of Cu. The Cu LMM Auger spectrum (Fig. S18) exhibited a prominent peak at 916.9 eV and a weaker peak at 918.9 eV, confirming the presence of Cu<sup>+</sup> and Cu<sup>0</sup> species in CuSA/AC-C<sub>3</sub>N<sub>4</sub> and CuAC-C<sub>3</sub>N<sub>4</sub>. In contrast, CuSA-C<sub>3</sub>N<sub>4</sub> exclusively demonstrated the Cu<sup>+</sup> species. Single-atom sites typically exhibited a higher oxidation state for metals than nanoparticles. Meanwhile, atom clusters could be viewed as transitional structures between single atoms and nanoparticles, resulting in an average metal valence state that fell in between. Thus, the existence of atom clusters, compared to the "Sea" structure of individual single atoms, was supported at the electron level by a decrease in binding energy and the average valence state of Cu [64]. Due to the electron effect between the Islands and the Sea (named the Island-sea effect), the electron transfer from Cu-N to Cu-Cu in CuSA/AC-C<sub>3</sub>N<sub>4</sub> increased the number of charges and aggregation of the atom clusters, promoting its evolution into an "Island" with high reducibility.

To demonstrate the validity of the Island-sea structure of Cu in CuSA/AC-C<sub>3</sub>N<sub>4</sub>, the average valence state and the fine coordination environment of Cu were further determined by X-ray absorption spectroscopy (XAS). The Cu K-edge X-ray absorption near-edge structure (XANES) in Fig. 2c revealed that the Cu K-edge position (8982.8 eV) of CuSA/AC-C<sub>3</sub>N<sub>4</sub> lay between that of CuPc (8985.6 eV) and Cu<sub>2</sub>O (8982.55 eV). Additional fitting results (Fig. S19) showed the oxidation states of Cu in

CuSA/AC-C<sub>3</sub>N<sub>4</sub> and CuPc (Cu single atoms) were 1.07 + and 1.79 +, respectively, consistent with the average valence states of Cu obtained by XPS. The presence of Cu atom clusters in CuSA/AC-C<sub>3</sub>N<sub>4</sub> caused the K-edge position of Cu to shift from CuPc toward Cu foil and the valence state decreased to slightly above +1. Furthermore, the local structure of Cu in CuSA/AC-C<sub>3</sub>N<sub>4</sub> was investigated using EXAFS spectroscopy. First, the comparison with the standard sample determined that (Fig. S20), the highest peak in the first shell was assigned to Cu-N bonds, while the second shell was designated as Cu-Cu bonds in CuSA/AC-C<sub>3</sub>N<sub>4</sub>, representing the presence of Cu single atoms and Cu atom clusters, respectively. The two shells were slightly farther away than when they existed separately, suggesting interactions and electron effects between atom clusters and single atoms in the Island-sea structure. Additionally, the EXAFS spectra of other samples were fitted (Fig. 2d and Figs. S21-S23). Both Cu-Cu shells and Cu-N shells existed in CuAC-C<sub>3</sub>N<sub>4</sub>, while only the Cu-N shell was present in CuSA-C<sub>3</sub>N<sub>4</sub>. Moreover, the model-based EXAFS fitting of Cu K-edges (Table S4) revealed that the coordination numbers of Cu-Cu and Cu-N were 2.8 and 3.3, respectively. Subsequently, wavelet transforms (WT) with k and R space resolution were employed to examine the intricate configuration of the Cu Island-sea structure. In Fig. 2e, the highest strength of CuSA/AC-C<sub>3</sub>N<sub>4</sub> in the WT contour matched the Cu-Cu bonds and Cu-N bonds, conforming to the coexistence of Cu single atoms and atom clusters. The bond lengths of Cu-N and Cu-Cu in CuSA/AC-C<sub>3</sub>N<sub>4</sub> were different from those in CuPc and Cu foil. Importantly, the strongest oscillation signal (k values) for atoms with the same coordination for CuSA/AC-C<sub>3</sub>N<sub>4</sub> changed in the opposite direction, indicating potential electron effects between them. The figures of wavelet transform of CuSA-C<sub>3</sub>N<sub>4</sub> and CuAC-C<sub>3</sub>N<sub>4</sub> were shown in Fig. S24. The DFT calculations were utilized to explore the interaction and electron distribution between atom clusters and single atoms in the Island-sea structure. The optimized CuSA/AC-C<sub>3</sub>N<sub>4</sub>

structural model (Fig. 2f) based on the coordination fitting calculation results showed that there was electron accumulation between Cu single atom and atom cluster. The pyridine nitrogen in the middle of the island sea structure served as the electron transfer center connecting the single atom site and the atom cluster site, forming an electron bridge. Importantly, the electronic bridge formed by these accumulated electrons was the key to the island-sea structure. The presence of single atoms around the atom cluster led to a much higher charge accumulation in  $\text{Cu}_{\text{SA}}/\text{AC}-\text{C}_3\text{N}_4$  than that in pure atom clusters in  $\text{Cu}_{\text{AC}}-\text{C}_3\text{N}_4$  (Fig. S25), consistent with the earlier XPS results. As the results of various characterizations, the Island-sea structure changed the electronic and bonding properties of atom clusters and single atoms, all of which cooperatively formed the Island-sea effect.

### 3.2. Electrocatalytic $\text{CO}_2\text{RR}$ performance evaluation

Catalysts/CP obtained by loading catalysts ink on carbon paper (CP) with a single-sided hydrophobic PTFE layer was utilized for performance comparison. The electrocatalytic activities of  $\text{Cu}-\text{C}_3\text{N}_4$ ,  $\text{Cu}_{\text{SA}}-\text{C}_3\text{N}_4$ ,  $\text{Cu}_{\text{SA}}/\text{AC}-\text{C}_3\text{N}_4$ , and  $\text{Cu}_{\text{AC}}-\text{C}_3\text{N}_4$  for  $\text{CO}_2\text{RR}$  were evaluated in 0.1 M  $\text{CO}_2$ -saturated  $\text{KHCO}_3$  aqueous solution. The LSV curve in

Fig. 3a showed that  $\text{Cu}_{\text{SA}}/\text{AC}-\text{C}_3\text{N}_4$  exhibited the lowest current starting potential and began to separate at approximately  $-0.9$  V vs. RHE, which was subsequently determined as the starting potential of the  $\text{CO}_2\text{RR}$ . Additionally, by comparing the experiments in the Ar and  $\text{CO}_2$  environment, it was determined that the decreased current mainly originated from  $\text{CO}_2$  reduction, which further showed that the  $\text{C}_2\text{H}_4$  product came from  $\text{CO}_2$ . The current density was generally influenced by the amount of metal loading, but the current density of  $\text{Cu}_{\text{SA}}/\text{AC}-\text{C}_3\text{N}_4$  was significantly higher than that of  $\text{Cu}_{\text{AC}}-\text{C}_3\text{N}_4$ , suggesting its superior electrochemical performance countering the impact of the loading amount. Subsequently, all catalysts were electrostatic electrolysis as cathodes to evaluate the reduction products at various potentials between  $-1.08$  and  $-1.58$  V vs. RHE. The gaseous products of  $\text{CO}_2\text{RR}$  on all Cu catalysts were analyzed by gas chromatography (GC) (The main data of the experimental group included original data table of  $\text{CO}_2$  reduction, the GC images of  $\text{CO}_2$  reduction products, and the  $\text{H}_2$  chromatograms were shown in Figs. S26-S38) and converted to Faraday efficiency (FEs). As demonstrated in Fig. 3b,  $\text{Cu}_{\text{SA}}/\text{AC}-\text{C}_3\text{N}_4$  exhibited a remarkable selectivity of up to 80.73 % for  $\text{C}_2\text{H}_4$  at  $-1.28$  V vs. RHE. Furthermore, the  $\text{FEC}_2\text{H}_4$  of  $\text{Cu}_{\text{SA}}/\text{AC}-\text{C}_3\text{N}_4$  from  $-1.08$  to  $-1.58$  V vs. RHE was  $> 50$  %. Equally,  $^1\text{H}$  nuclear magnetic resonance ( $^1\text{H}$  NMR)

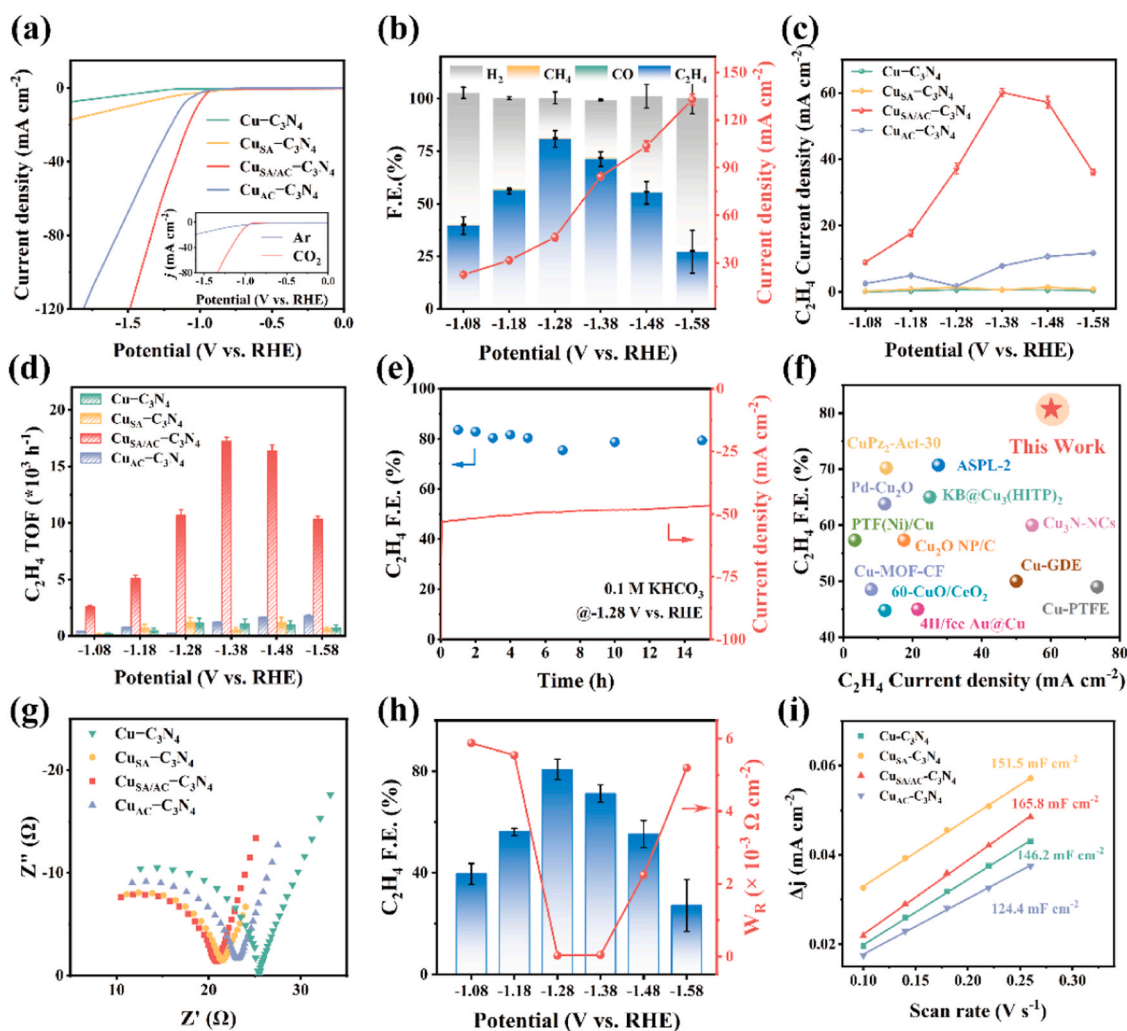


**Fig. 3.** (a) LSV curves of the prepared catalysts measured in  $\text{CO}_2$ -saturated 0.1 M  $\text{KHCO}_3$  electrolyte. Inset: LSV curves of  $\text{Cu}_{\text{SA}}/\text{AC}-\text{C}_3\text{N}_4$  obtained in Ar- and  $\text{CO}_2$ -saturated 0.1 M  $\text{KHCO}_3$ . (b) FE of different products for  $\text{Cu}_{\text{SA}}/\text{AC}-\text{C}_3\text{N}_4$  at different applied potentials. (c) Partial current density of  $\text{C}_2\text{H}_4$ , and (d) Calculated TOF value for  $\text{Cu}-\text{C}_3\text{N}_4$ ,  $\text{Cu}_{\text{SA}}-\text{C}_3\text{N}_4$ ,  $\text{Cu}_{\text{SA}}/\text{AC}-\text{C}_3\text{N}_4$  and  $\text{Cu}_{\text{AC}}-\text{C}_3\text{N}_4$  at different applied potentials. (e) Stability test for  $\text{Cu}_{\text{SA}}/\text{AC}-\text{C}_3\text{N}_4$  at  $-1.28$  V vs. RHE with 15 h of continuous operation. (f) Comparison chart of the corresponding  $\text{C}_2\text{H}_4$  current density at the potential of the highest FE of  $\text{C}_2\text{H}_4$ . (g) The EIS plot for different samples. (h) The relationship between diffusion impedance ( $W_R$ ), applied potential, and selectivity of  $\text{C}_2\text{H}_4$  for  $\text{Cu}_{\text{SA}}/\text{AC}-\text{C}_3\text{N}_4$ . (i) The  $\text{C}_{\text{dl}}$  of  $\text{Cu}-\text{C}_3\text{N}_4$ ,  $\text{Cu}_{\text{SA}}-\text{C}_3\text{N}_4$ ,  $\text{Cu}_{\text{SA}}/\text{AC}-\text{C}_3\text{N}_4$  and  $\text{Cu}_{\text{AC}}-\text{C}_3\text{N}_4$  were calculated with changes in current density and sweep rate, respectively.



spectroscopy (Figs. S39 and S40) analyzed the liquid products of Cu–C<sub>3</sub>N<sub>4</sub> and Cu<sub>SA</sub>/AC–C<sub>3</sub>N<sub>4</sub> at  $-1.18$  V vs. RHE, in which no other liquid species peaks appeared except solvent peaks (DMSO) and water peaks [65]. Therefore, liquid products were not included in CO<sub>2</sub>RR reduction products. Additionally, trace amounts of CH<sub>4</sub> and CO as by-products in Cu<sub>SA</sub>/AC–C<sub>3</sub>N<sub>4</sub> and Cu<sub>AC</sub>–C<sub>3</sub>N<sub>4</sub> were also negligible. Throughout the applied potential range, the Cu<sub>SA</sub>/AC–C<sub>3</sub>N<sub>4</sub> electrode showed unprecedented CO<sub>2</sub> reduction selectivity for C<sub>2</sub>H<sub>4</sub>, as more than 99.4 % of CO<sub>2</sub> reduction products were C<sub>2</sub>H<sub>4</sub>. Moreover, the partial current density of C<sub>2</sub>H<sub>4</sub> (Fig. 3c) was calculated to assess their potential for industrial application. For Cu<sub>SA</sub>/AC–C<sub>3</sub>N<sub>4</sub>, the maximum partial current density of C<sub>2</sub>H<sub>4</sub> reached  $60.14 \text{ mA cm}^{-2}$  at  $-1.38$  V vs. RHE. Cu<sub>SA</sub>/AC–C<sub>3</sub>N<sub>4</sub> demonstrated an overwhelming advantage over other catalysts in C<sub>2</sub>H<sub>4</sub> partial current density at the potential window for the experiments. As for Cu<sub>SA</sub>–C<sub>3</sub>N<sub>4</sub>, the maximum FE for C<sub>2</sub>H<sub>4</sub> was only 20 % (Fig. S41). Although the Cu<sub>AC</sub>–C<sub>3</sub>N<sub>4</sub> also exhibited acceptable C<sub>2</sub>H<sub>4</sub> selectivity (less than 50 %) and total current density, Cu<sub>SA</sub>/AC–C<sub>3</sub>N<sub>4</sub> had a maximum C<sub>2</sub>H<sub>4</sub> current density of up to 22 times that of the former at same applied potential. To eliminate the effect of metal loading on current density, the TOF values of the catalysts were calculated to determine the intrinsic activity of the catalytic center. The developed Cu<sub>SA</sub>/AC–C<sub>3</sub>N<sub>4</sub> catalyst exhibited an extremely high TOF of  $17000 \text{ h}^{-1}$  at  $-1.38$  V vs. RHE, outperforming most of the state-of-the-art catalysts evaluated under similar applications (Fig. 3d and Table S5). Beyond that, the Cu<sub>SA</sub>/AC–C<sub>3</sub>N<sub>4</sub> electrocatalyst had outstanding long-term catalytic stability and life, revealing no substantial current decay and nearly constant FE of C<sub>2</sub>H<sub>4</sub> over 15 h continuous operation (Fig. 3e). Subsequently, the determination of the catalyst after the reaction by XRD, FT-IR and HAADF-STEM confirmed that its crystal structure, functional groups and active sites were not significantly changed due to the long-term reaction (Figs. S42–S44). The brilliant stability of Cu<sub>SA</sub>/AC–C<sub>3</sub>N<sub>4</sub> could be attributed to the Island-sea effect, which not only enhanced the strong coupling interaction between Cu atomic clusters and single atoms with the coordinated N atoms in the surrounding, but also increased the repulsive force between metal centers, thus maintaining the stability and dispersion of the metal active sites. Comparing to the highest values of FE and current density of C<sub>2</sub>H<sub>4</sub> in the literature (Fig. 3f and Table S6), Cu<sub>SA</sub>/AC–C<sub>3</sub>N<sub>4</sub> exhibited ultra-high activity for CO<sub>2</sub>RR and selectivity towards C<sub>2</sub>H<sub>4</sub>.

To reveal the reaction kinetic characteristics of the catalysts, a series of electrochemical characterizations were conducted. The higher tafel slopes (Fig. S45) of Cu–C<sub>3</sub>N<sub>4</sub> ( $561.01 \text{ mV dec}^{-1}$ ) and Cu<sub>SA</sub>–C<sub>3</sub>N<sub>4</sub> ( $402.0 \text{ mV dec}^{-1}$ ) determined under CO<sub>2</sub>RR conditions demonstrated the weak catalytic activity of single atoms in producing C<sub>2</sub>H<sub>4</sub>. However, the smallest slope of Cu<sub>SA</sub>/AC–C<sub>3</sub>N<sub>4</sub> ( $125.09 \text{ mV dec}^{-1}$ ) had the greatest growth potential for current density, determining the enhanced kinetics of its CO<sub>2</sub> conversion. Electrochemical impedance spectroscopy (EIS) measurements at open-circuit potential further confirmed the improved kinetic activity of Cu<sub>SA</sub>/AC–C<sub>3</sub>N<sub>4</sub>, as it displayed the smallest radius representing the fastest electron transfer (Fig. 3g and Table S7). In previous studies, the activation of H<sub>2</sub>O and protonation processes were found to accelerate kinetics, so the coverage of adsorbed hydrogen (\*H) on the catalyst surface was studied by in-situ EIS measurements to explore the relationship between the kinetics and behaviors of different species on the surface of catalysts [66,67]. Unfortunately, affected by the mass transfer process (the coverage of \*H was masked as diffusion impedance, also known as Warburg impedance,  $W_R$ ), only Cu–C<sub>3</sub>N<sub>4</sub> can simulate the Nyquist plot using a double parallel equivalent circuit model. The specific fitting parameters were shown in Fig. S46 and Table S8, where adsorption pseudocapacitance ( $C_n$ ) of Cu–C<sub>3</sub>N<sub>4</sub> was used to define the coverage of \*H involving charge adsorption. The results showed that the  $C_n$  value associated with coverage of \*H was particularly tiny and only increased slightly as the applied potential increased, corroborating its poor intrinsic activity. To supplement the above experiments, the EIS results of Cu<sub>SA</sub>–C<sub>3</sub>N<sub>4</sub>, Cu<sub>SA</sub>/AC–C<sub>3</sub>N<sub>4</sub>, and Cu<sub>AC</sub>–C<sub>3</sub>N<sub>4</sub> at the reaction potential were fitted with the diffusion

impedance (Fig. S47, after the internal resistance  $R_1$ ,  $C_n$  was replaced with a diffusion resistance element, which represented the resistance of the substance when it separated from the surface of catalysts). Surprisingly, there was a correlation between diffusion impedance in different catalysts and FE of C<sub>2</sub>H<sub>4</sub>. For Cu<sub>SA</sub>–C<sub>3</sub>N<sub>4</sub>, the FE of C<sub>2</sub>H<sub>4</sub> showed a strong positive linear relationship with its diffusion impedance and  $R^2$  was up to 0.97, which presented that the increase of diffusion impedance was conducive to deep reduction of CO<sub>2</sub> (Fig. S48 and Table S9). Conversely, diffusion impedance of Cu<sub>SA</sub>/AC–C<sub>3</sub>N<sub>4</sub>, and Cu<sub>AC</sub>–C<sub>3</sub>N<sub>4</sub> was negatively correlated with FE of C<sub>2</sub>H<sub>4</sub> ( $R^2 = 0.96$ , Fig. 3h, Figs. S49, S50 and Table S10). And all fitted graphs were presented in Figs. S51–S54. The increased diffusion impedance hampered the synthesis of C<sub>2</sub>H<sub>4</sub>, suggesting that for the catalysts with the atom cluster, there may be a mass transfer step of the intermediate, which might even be the rate-limiting step of the reaction. It should be noted that the diffusion impedance was also influenced by the applied potential, as seen in the three catalysts (points outside the fitted curve). Increasing the applied potential would reduce the diffusion impedance, so two points with a wide potential gap were unsuitable for direct comparison. For example, the FE of C<sub>2</sub>H<sub>4</sub> for Cu<sub>SA</sub>–C<sub>3</sub>N<sub>4</sub> at  $-1.08$  and  $-1.58$  V vs. RHE was similar, but the diffusion impedance at  $-1.58$  V vs. RHE was lower. To further compare the intrinsic activities of Cu<sub>SA</sub>–C<sub>3</sub>N<sub>4</sub>, Cu<sub>SA</sub>/AC–C<sub>3</sub>N<sub>4</sub>, Cu<sub>AC</sub>–C<sub>3</sub>N<sub>4</sub>, and Cu–C<sub>3</sub>N<sub>4</sub>, cyclic voltammetry was measured at various scan rates ( $100\text{--}260 \text{ mV s}^{-1}$ ) to determine their electrochemical active surface area (ECSA) by calculating the double layer capacitance ( $C_{dl}$ ) (Fig. S55). As the performance suggested, Cu<sub>SA</sub>/AC–C<sub>3</sub>N<sub>4</sub> had the highest  $C_{dl}$  (Fig. 3i), representing its large active surface area, which considerably benefited from the increased density and exposure of active sites conferred by the Island-sea effect.

### 3.3. Exploration of the CO<sub>2</sub> reduction pathways

The SERS was employed to detect intermediates during the CO<sub>2</sub>RR process (Fig. 4a,b, and Fig. S56). Before the reaction, two characteristic bands at  $385$  and  $423 \text{ cm}^{-1}$  were observed, which was attributed to Cu–N in Cu<sub>SA</sub>/AC–C<sub>3</sub>N<sub>4</sub> [68–70]. Two other bands near  $1364$  and  $1610 \text{ cm}^{-1}$  were identified as characteristic peaks of the carbon paper (D and G peaks). Upon introducing CO<sub>2</sub>-saturated KHCO<sub>3</sub> electrolyte into the reactor, the D and G peaks of the carbon paper were overshadowed by the strong characteristic peak of \*CO<sub>2</sub> in proximity, demonstrating the high CO<sub>2</sub> adsorption capacity of Cu<sub>SA</sub>/AC–C<sub>3</sub>N<sub>4</sub>. Despite the close proximity of the characteristic peaks of \*CO<sub>2</sub> and the D peak of C, the observed blue shift and pronounced signal enhancement unequivocally attribute these changes to the \*CO<sub>2</sub>. Applying a scanning potential ranging from  $-1.08$  to  $-1.68$  V vs. RHE on Cu<sub>SA</sub>/AC–C<sub>3</sub>N<sub>4</sub>, the characteristic peak of \*CO<sub>2</sub> significantly weakened and underwent a blue shift from  $1350$  to  $1380 \text{ cm}^{-1}$  as the applied potential became negative for stacking effect, corresponding to increased \*CO<sub>2</sub> activation. Crucially, several characteristic bands representing intermediate species emerged at the onset of the reaction, providing valuable insights into the CO<sub>2</sub>RR process. The red and blue shift of the Cu–N characteristic peaks to  $381$  and  $451 \text{ cm}^{-1}$ , respectively, matched Cu–C stretching and Cu–CO, suggesting that CO may originate from Cu single atom sites [20]. The slight blue shift of the Cu–H characteristic peak at approximately  $580 \text{ cm}^{-1}$  implied an increase in adsorption strength with increasing potential. Furthermore, based on previous reports, the bands at  $\sim 431 \text{ cm}^{-1}$  and  $1600\text{--}1640 \text{ cm}^{-1}$  likely fell into C(H)O species, with the former being the Cu–C(H)O characteristic peak on Cu sites and the larger shift range of the latter, indicating the possible presence of C(H)O adsorption on different sites, such as Cu single atom and Cu cluster sites [71]. The characteristic peaks at  $645$  and  $751 \text{ cm}^{-1}$  belonged to \*OH species [72]. The blue shift of the characteristic peak at  $751 \text{ cm}^{-1}$  with the application of negative potential demonstrated that it may depict not only H<sub>2</sub>O but also hydroxyl-containing intermediate species following the reduction reaction. Importantly, the characteristic peak at  $420 \text{ cm}^{-1}$  that may represent Cu–C<sub>2</sub>, indicated the generation of C<sub>2</sub> intermediates

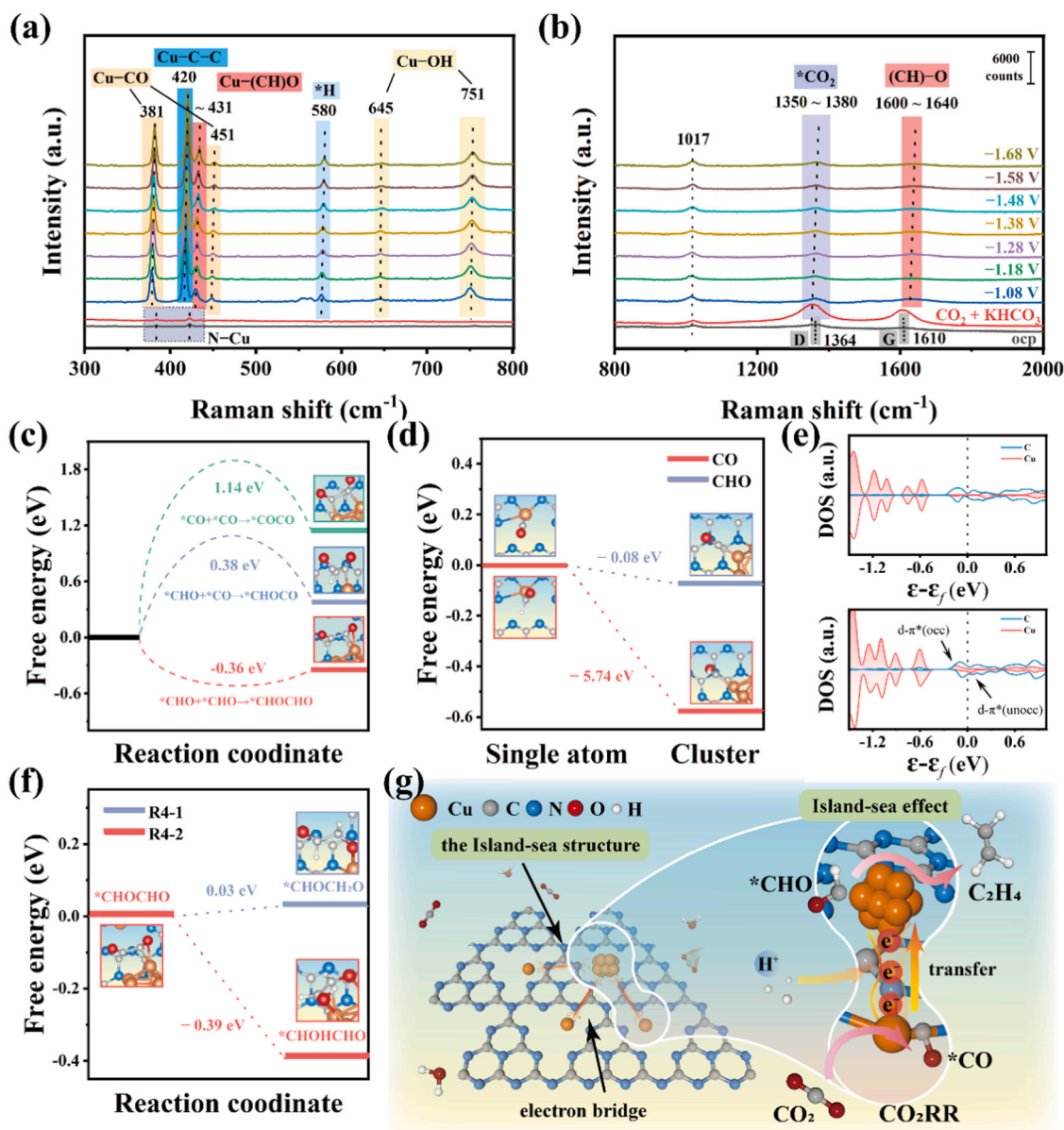


**Fig. 4.** (a) The in-situ surface-enhanced Raman spectroscopy of Cu<sub>SA/AC</sub>-C<sub>3</sub>N<sub>4</sub> in (a) 300–800 and (b) 800–2000 cm<sup>-1</sup>, respectively. (c) The energy required for the coupling process of C<sub>1</sub> different intermediates. (d) The free energy of transfer for \*CO and \*CHO from Cu single atom site to atom cluster site. (e) The PDOS of Cu<sub>SA/AC</sub>-C<sub>3</sub>N<sub>4</sub> and Cu<sub>SA/AC</sub>-C<sub>3</sub>N<sub>4</sub>-CHO (\*CHO on atom cluster site). (f) The free energy of R4-1 and R4-2 on atom cluster site for Cu<sub>SA/AC</sub>-C<sub>3</sub>N<sub>4</sub> when electrons were supplied from the electron bridge. (g) Schematic diagram of the electrocatalytic reduction of CO<sub>2</sub> to C<sub>2</sub>H<sub>4</sub> on Cu<sub>SA/AC</sub>-C<sub>3</sub>N<sub>4</sub>.

and products. The spectral band of the C<sub>1</sub> and C<sub>2</sub> intermediate (381, 420, and 431 cm<sup>-1</sup>) showed enhanced intensity with negative applied potential, indicating continuous generation and accumulation. Based on the in-situ Raman results, it can be assumed that CO<sub>2</sub> was adsorbed by the Cu<sub>SA/AC</sub>-C<sub>3</sub>N<sub>4</sub> before the potential was applied. Once the reaction began, the \*CO<sub>2</sub> was first preliminarily reduced to CO at the Cu single-atom sites. Subsequently, the C<sub>1</sub> intermediates may undergo diffusion and transfer steps, culminating in the formation of C<sub>2</sub>H<sub>4</sub> at suitable sites such as Cu atom cluster sites.

### 3.4. Performance improvement mechanism of Island-sea effect

To further elucidate the excellent selectivity and efficiency of C<sub>2</sub>H<sub>4</sub> production under the Island-sea structure and the mode of action of the Island-sea effect, DFT calculations were performed. Based on the characterization of the prepared catalysts, three different models were constructed to simulate Cu<sub>SA</sub>-C<sub>3</sub>N<sub>4</sub>, Cu<sub>SA/AC</sub>-C<sub>3</sub>N<sub>4</sub>, and Cu<sub>AC</sub>-C<sub>3</sub>N<sub>4</sub>

(Fig. S24). The number of atoms in the Cu cluster was chosen as 10, based on the ligands proportion used in synthesis. Usually, the C-C coupling step was the key to producing C<sub>2</sub> + products, so the most favorable coupling pathway on the built model was first explored. Considering the in-situ Raman test and the generally high selectivity of C<sub>2</sub>H<sub>4</sub> for catalysts containing Cu clusters, Cu atom clusters were identified as the primary coupling sites for C<sub>2</sub> + products, while Cu single atoms have consistently been recognized as the active sites in single-atom catalysts. Several possible C-C coupling pathways were considered, including \*CO + \*CO, \*CO + \*CHO, \*CHO + \*CHO, with corresponding energies of 1.14 eV, 0.38 eV, and -0.36 eV, respectively (Fig. 4c). Among them, \*CHO + \*CHO exhibited the lowest energy, so \*CHO was chosen as the basis for subsequent simulations and its origin was explored as a key intermediate. The characteristic peaks of Cu-CHO and Cu-CO in in-situ Raman spectroscopy suggested that a portion of \*CHO was expected to originate from Cu single-atom sites. The characterization and performance results also demonstrated that the



exceptional C<sub>2</sub>H<sub>4</sub> selectivity of Cu<sub>SA/AC</sub>-C<sub>3</sub>N<sub>4</sub> cannot be attributed to the action of a single type of active site. Additionally, in-situ EIS measurements have revealed a strong correlation between diffusion impedance and C<sub>2</sub>H<sub>4</sub> production, revealing that the reaction intermediate was likely migrated to the atom clusters via electronic bridges in the Island-sea structure for subsequent reactions. Therefore, the free energy of migration for \*CHO and \*CO on the surface of Cu<sub>SA/AC</sub>-C<sub>3</sub>N<sub>4</sub> was calculated in the migration direction from Cu single atom site to Cu atom cluster site. As shown in Fig. 4d, the free energy of migration for \*CHO from Cu atom site to atom cluster site was lower, proving that in the CO<sub>2</sub>RR process, \*CHO was first generated on Cu single atom sites (R1+R2) and then transferred to Cu atom clusters sites for coupling (R3).



The high reducibility resulting from electron accumulation was considered a crucial factor favoring the coupling reaction, as observed from the distribution of products in CO<sub>2</sub>RR experiments. To gain deeper insights into the electronic properties, the density of states (DOS) of different Cu species was further analyzed to investigate the electronic distribution of orbital energy levels (Fig. 4e). In the absence of the coupling species \*CHO, the d orbital of Cu above the fermi level in Cu<sub>SA/AC</sub>-C<sub>3</sub>N<sub>4</sub> was situated far from it, favoring the activation of CO<sub>2</sub>, which was corresponded to a more active state. However, upon adsorption of the coupling species \*CHO, the d-π \* orbital above the fermi level of Cu<sub>SA/AC</sub>-C<sub>3</sub>N<sub>4</sub> fell near the fermi level due to the strong adsorption and activation of \*CHO. The d-π \* orbitals of \*CHO adsorbed at the Cu single atom site in Cu<sub>SA/AC</sub>-C<sub>3</sub>N<sub>4</sub> were all positioned below the Fermi level (Fig. S57), which was a manifestation of weak adsorption. This further demonstrated the possibility of intermediates being transported from single-atom sites and atom cluster sites. Therefore, the high electron activity of the atom cluster facilitated better adsorption and activation of intermediate species, driving the reaction towards deeper reduction products.

However, these factors alone were insufficient to explain the high selectivity of Cu<sub>SA/AC</sub>-C<sub>3</sub>N<sub>4</sub> towards C<sub>2</sub>H<sub>4</sub>, as the enhanced C-C coupling step would also favor the formation of other C<sub>2</sub> products. The hydrogenation of \*CHOCHO also played an indispensable role in the C<sub>2</sub>-targeted reduction pathway R4 [71]. As shown in Table S11, there was a significant difference in the adsorption energy of \*H among different Cu species. Cu single atoms exhibited excellent \*H aggregation ability, while \*H adsorption on Cu atom clusters was relatively weak, which was also a prerequisite for the outstanding coupling ability of atom clusters. Actually, the Island-sea structure not only facilitated the coupling pathway by migration of \*CHO, but also modified the subsequent hydrogenation process on the catalyst surface, which was the result of optimizing the interfacial effect.



Specifically, the electronic bridges in the Island-sea structure not only facilitated the migration of \*CHO, but also promoted the migration of \*H from Cu single atom to cluster and even directly aggregated \*H from the electrolyte. It compensated for the weak adsorption capacity of the cluster for \*H. The selectivity and reaction rate of the R4 pathway was influenced by the source of \*H. When \*H was obtained from the electronic bridge for hydrogenation, the free energy of R4-1 increased (from -0.16 eV to 0.03 eV), and the free energy of R4-2 decreased (from -0.34 eV to -0.39 eV) (Fig. 4f and Fig. S58). The increased free energy gap demonstrated the promotion of the C<sub>2</sub>H<sub>4</sub> pathway and the relative suppression of the CH<sub>3</sub>COOH pathway, resulting in enhanced

C<sub>2</sub>H<sub>4</sub> selectivity. The interfacial effect significantly affected the hydrogenation position to improve the selectivity of the pathway and further increased the energy gap, thereby promoting the pathway of C<sub>2</sub>H<sub>4</sub>. Similarly, when the Cu atom cluster directly obtained \*H from the electrolyte, the free energy of R4-2 was lower than that of R4-1. Hence, the alteration in the \*H source did not result in the generation of CH<sub>3</sub>COOH, but rather contributed to the deceleration of the hydrogenation process and the enhancement of H<sub>2</sub> selectivity, which was in accordance with the performance exhibited by Cu<sub>AC</sub>-C<sub>3</sub>N<sub>4</sub>.

Overall, in Cu<sub>SA/AC</sub>-C<sub>3</sub>N<sub>4</sub>, the initial reduction of CO<sub>2</sub> took place on Cu single atom sites, generating \*CHO, which then migrated to Cu atom clusters for subsequent coupling and hydrogenation reactions. The Island-sea structure provided suitable interface effects, further enhancing the selectivity of C<sub>2</sub>H<sub>4</sub>. The \*CHO and \*H were continuously transported from the Sea to Island by a conveyor belt-like electron bridge for production of C<sub>2</sub>H<sub>4</sub>, contributing to the impressive selectivity and efficiency for C<sub>2</sub>H<sub>4</sub> of Cu<sub>SA/AC</sub>-C<sub>3</sub>N<sub>4</sub>.

#### 4. Conclusion

In summary, the highly dispersed Cu single-atom and atom cluster sites were precisely controlled through a dual-ligand chelation strategy, resulting in the targeted formation of Cu<sub>SA/AC</sub>-C<sub>3</sub>N<sub>4</sub> with an Island-sea structure. We have demonstrated the existence of the Island-sea structure and its Island-sea effect through a series of experiments and characterizations. The crucial intermediate \*CHO has initially been generated at Cu single-atom sites and then transferred to atom cluster sites through the electron bridge within the Island-sea structure for subsequent coupling and multi-step reduction. Moreover, the electron bridge connected successive multi-electron steps and unified the function of single atoms and clusters, in consequence of directing them toward excellent C<sub>2</sub>H<sub>4</sub> activity and selectivity. As a result, the Cu<sub>SA/AC</sub>-C<sub>3</sub>N<sub>4</sub> electrocatalyst with the unique Island-sea structure exhibited remarkable CO<sub>2</sub>RR activity (>17000 h<sup>-1</sup>) and selectivity (80.35 % for C<sub>2</sub>H<sub>4</sub> and carbonaceous products above 99.4 %). This study investigates the design of "single atom-cluster" reaction sites and provides profound insights into the mechanism of the Island-sea effect underlying the enhancement of CO<sub>2</sub>RR, thereby paving the way for the development of superior M-N-C catalysts.

#### CRedit authorship contribution statement

**Zhu Chao:** Conceptualization, Funding acquisition, Methodology, Supervision, Writing – review & editing. **Zhang Haizhong:** Conceptualization, Data curation, Formal analysis, Investigation, Methodology, Software, Validation, Visualization, Writing – original draft. **Song Shuang:** Writing – review & editing. **Shen Yi:** Conceptualization, Funding acquisition, Resources, Supervision, Writing – review & editing. **Liu Renlan:** Writing – review & editing. **Fang Qile:** Writing – review & editing.

#### Declaration of Competing Interest

The authors declare that they have no known competing financial interests or personal relationships that could have appeared to influence the work reported in this paper.

#### Data availability

Data will be made available on request.

#### Acknowledgements

This research was supported by the National Natural Science Foundation of China (22276171, 22006131), the Fundamental Research Funds for the Provincial Universities of Zhejiang (RF-C2023009), the

China Postdoctoral Science Foundation (2022M722811, 2020T130598, 2019M662106), the Zhejiang Provincial Natural Science Foundation of China (LQ20B070010, LQ20B070012), Zhuhai Science and Technology Bureau (ZH22017003210025PWC).

## Appendix A. Supporting information

Supplementary data associated with this article can be found in the online version at doi:10.1016/j.apcatb.2023.123566.

## References

- [1] Y.H. Zou, Y.B. Huang, D.H. Si, Q. Yin, Q.J. Wu, Z. Weng, R. Cao, Porous metal-organic framework liquids for enhanced CO<sub>2</sub> adsorption and catalytic conversion, *Angew. Chem. Int. Ed.* 60 (2021) 20915–20920.
- [2] Y. Wu, Z. Jiang, X. Lu, Y. Liang, H. Wang, Domino electroreduction of CO(2) to methanol on a molecular catalyst, *Nature* 575 (2019) 639–642.
- [3] Y.Y. Birdja, E. Pérez-Gallent, M.C. Figueiredo, A.J. Göttele, F. Calle-Vallejo, M.T. M. Koper, Advances and challenges in understanding the electrocatalytic conversion of carbon dioxide to fuels, *Nat. Energy* 4 (2019) 732–745.
- [4] X. Deng, D. Alfonso, T.-D. Nguyen-Phan, D.R. Kauffman, Resolving the size-dependent transition between CO<sub>2</sub> reduction reaction and H<sub>2</sub> evolution reaction selectivity in sub-5 nm silver nanoparticle electrocatalysts, *ACS Catal.* 12 (2022) 5921–5929.
- [5] M. Ding, R.W. Flaig, H.L. Jiang, O.M. Yaghi, Carbon capture and conversion using metal-organic frameworks and MOF-based materials, *Chem. Soc. Rev.* 48 (2019) 2783–2828.
- [6] L. Zhang, X.X. Li, Z.L. Lang, Y. Liu, J. Liu, L. Yuan, W.Y. Lu, Y.S. Xia, L.Z. Dong, D. Q. Yuan, Y.Q. Lan, Enhanced cuprophilic interactions in crystalline catalysts facilitate the highly selective electroreduction of CO<sub>2</sub> to CH<sub>4</sub>, *J. Am. Chem. Soc.* 143 (2021) 3808–3816.
- [7] L. Han, X. Liu, J. He, Z. Liang, H.T. Wang, S.M. Bak, J. Zhang, A. Hunt, I. Waluyo, W.F. Pong, J. Luo, Y. Ding, R.R. Adzic, H.L. Xin, Modification of the coordination environment of active sites on MoC for high-efficiency CH<sub>4</sub> production, *Adv. Energy Mater.* 11 (2021).
- [8] S. Mukhopadhyay, R. Shimoni, I. Liberman, R. Ifraimov, I. Rozenberg, I. Hod, Assembly of a metal-organic framework (MOF) membrane on a solid electrocatalyst: introducing molecular-level control over heterogeneous CO<sub>2</sub> reduction, *Angew. Chem. Int. Ed.* 60 (2021) 13423–13429.
- [9] D.L. Meng, M.D. Zhang, D.H. Si, M.J. Mao, Y. Hou, Y.B. Huang, R. Cao, Highly selective tandem electroreduction of CO<sub>2</sub> to ethylene over atomically isolated nickel-nitrogen site/copper nanoparticle catalysts, *Angew. Chem. Int. Ed.* 60 (2021) 25485–25492.
- [10] T. Zheng, K. Jiang, H. Wang, Recent advances in electrochemical CO<sub>2</sub> to-CO conversion on heterogeneous catalysts, *Adv. Mater.* 30 (2018), e1802066.
- [11] Y. Zhang, L. Jiao, W. Yang, C. Xie, H.L. Jiang, Rational fabrication of low-coordinate single-atom Ni electrocatalysts by MOFs for highly selective CO<sub>2</sub> reduction, *Angew. Chem. Int. Ed.* 60 (2021) 7607–7611.
- [12] Z.-Y. Zhang, H. Tian, L. Bian, S.-Z. Liu, Y. Liu, Z.-L. Wang, Cu-Zn-based alloy/oxide interfaces for enhanced electroreduction of CO<sub>2</sub> to C<sub>2</sub>+ products, *J. Energy Chem.* 83 (2023) 90–97.
- [13] D.D. Zhu, J.L. Liu, S.Z. Qiao, Recent advances in inorganic heterogeneous electrocatalysts for reduction of carbon dioxide, *Adv. Mater.* 28 (2016) 3423–3452.
- [14] H. Zhang, X. Chang, J.G. Chen, W.A. Goddard 3rd, B. Xu, M.J. Cheng, Q. Lu, Computational and experimental demonstrations of one-pot tandem catalysis for electrochemical carbon dioxide reduction to methane, *Nat. Commun.* 10 (2019) 3340.
- [15] E.L. Clark, C. Hahn, T.F. Jaramillo, A.T. Bell, Electrochemical CO<sub>2</sub> reduction over compressively strained CuAg surface alloys with enhanced multi-carbon oxygenate selectivity, *J. Am. Chem. Soc.* 139 (2017) 15848–15857.
- [16] J. Gao, H. Zhang, X. Guo, J. Luo, S.M. Zakeeruddin, D. Ren, M. Gratzel, Selective C-C coupling in carbon dioxide electroreduction via efficient spillover of intermediates As supported by Operando Raman spectroscopy, *J. Am. Chem. Soc.* 141 (2019) 18704–18714.
- [17] M. Luo, J. Yang, X. Li, M. Eguchi, Y. Yamauchi, Z.-L. Wang, Insights into alloy/oxide or hydroxide interfaces in Ni-Mo-based electrocatalysts for hydrogen evolution under alkaline conditions, *Chem. Sci.* 14 (2023) 3400–3414.
- [18] C. Chen, Y. Li, S. Yu, S. Louisia, J. Jin, M. Li, M.B. Ross, P. Yang, Cu-Ag tandem catalysts for high-rate CO<sub>2</sub> electrolysis toward multicarbons, *Joule* 4 (2020) 1688–1699.
- [19] J. Du, S. Li, S. Liu, Y. Xin, B. Chen, H. Liu, B. Han, Selective electrochemical reduction of carbon dioxide to ethanol via a relay catalytic platform, *Chem. Sci.* 11 (2020) 5098–5104.
- [20] Y. Zhao, X. Chang, A.S. Malkani, X. Yang, L. Thompson, F. Jiao, B. Xu, Speciation of Cu surfaces during the electrochemical CO reduction reaction, *J. Am. Chem. Soc.* 142 (2020) 9735–9743.
- [21] H. Bao, Y. Qiu, X. Peng, J.A. Wang, Y. Mi, S. Zhao, X. Liu, Y. Liu, R. Cao, L. Zhuo, J. Ren, J. Sun, J. Luo, X. Sun, Isolated copper single sites for high-performance electroreduction of carbon monoxide to multicarbon products, *Nat. Commun.* 12 (2021) 238.
- [22] D. Wakerley, S. Lamaison, F. Ozanam, N. Menguy, D. Mercier, P. Marcus, M. Fontecave, V. Mougél, Bio-inspired hydrophobicity promotes CO<sub>2</sub> reduction on a Cu surface, *Nat. Mater.* 18 (2019) 1222–1227.
- [23] Y. Chen, P. Wang, H. Hao, J. Hong, H. Li, S. Ji, A. Li, R. Gao, J. Dong, X. Han, M. Liang, D. Wang, Y. Li, Thermal atomization of platinum nanoparticles into single atoms: an effective strategy for engineering high-performance nanozymes, *J. Am. Chem. Soc.* 143 (2021) 18643–18651.
- [24] E. Perez-Gallent, M.C. Figueiredo, F. Calle-Vallejo, M.T. Koper, Spectroscopic observation of a hydrogenated CO dimer intermediate during CO reduction on Cu (100) electrodes, *Angew. Chem. Int. Ed.* 56 (2017) 3621–3624.
- [25] Y. Yang, I.B. Perry, G. Lu, P. Liu, S.L. Buchwald, Thermally stable single-atom platinum-on-ceria catalysts via atom trapping, *Science* 353 (2016) 144–150.
- [26] X. Gong, P. Song, C. Han, Y. Xiao, X. Mei, W. Xu, Heterogeneous single-atom catalysts for energy process: recent progress, applications and challenges, *Energy Mater.* 3 (2023), 300016.
- [27] H. Wang, Y.K. Tzeng, Y. Ji, Y. Li, J. Li, X. Zheng, A. Yang, Y. Liu, Y. Gong, L. Cai, Y. Li, X. Zhang, W. Chen, B. Liu, H. Lu, N.A. Melosh, Z.X. Shen, K. Chan, T. Tan, S. Chu, Y. Cui, Synergistic enhancement of electrocatalytic CO<sub>2</sub> reduction to C<sub>2</sub> oxygenates at nitrogen-doped nanodiamonds/Cu interface, *Nat. Nanotechnol.* 15 (2020) 131–137.
- [28] J.X. Wu, S.Z. Hou, X.D. Zhang, M. Xu, H.F. Yang, P.S. Cao, Z.Y. Gu, Cathodized copper porphyrin metal-organic framework nanosheets for selective formate and acetate production from CO<sub>2</sub> electroreduction, *Chem. Sci.* 10 (2019) 2199–2205.
- [29] J. Yang, X. Wang, Y. Qu, X. Wang, H. Huo, Q. Fan, J. Wang, L.M. Yang, Y. Wu, Bi-based metal-organic framework derived leafy bismuth nanosheets for carbon dioxide electroreduction, *Adv. Energy Mater.* 10 (2020).
- [30] K. Yao, Y. Xia, J. Li, N. Wang, J. Han, C. Gao, M. Han, G. Shen, Y. Liu, A. Seifitokaldani, X. Sun, H. Liang, Metal-organic framework derived copper catalysts for CO<sub>2</sub> to ethylene conversion, *J. Mater. Chem. A* 8 (2020) 11117–11123.
- [31] S.Y. Lee, H. Jung, N.K. Kim, H.S. Oh, B.K. Min, Y.J. Hwang, Mixed copper states in anodized Cu electrocatalyst for stable and selective ethylene production from CO<sub>2</sub> reduction, *J. Am. Chem. Soc.* 140 (2018) 8681–8689.
- [32] F. Yang, P. Deng, Q. Wang, J. Zhu, Y. Yan, L. Zhou, K. Qi, H. Liu, H.S. Park, B. Y. Xia, Metal-organic framework-derived cupric oxide polycrystalline nanowires for selective carbon dioxide electroreduction to C<sub>2</sub> valuables, *J. Mater. Chem. A* 8 (2020) 12418–12423.
- [33] U.N. Pan, D.R. Paudel, A. Kumar Das, T.I. Singh, N.H. Kim, J.H. Lee, Ni-nanoclusters hybridized 1T-Mn-VTe<sub>2</sub> mesoporous nanosheets for ultra-low potential water splitting, *Appl. Catal. B Environ.* 301 (2022).
- [34] G. Han, W. Zhang, L. Li, J. Du, Y. Yan, L. Geng, Y. Tong, C. Du, Progress in the high-temperature synthesis of atomically dispersed metal on carbon and understanding of their formation mechanism, *Energy Mater.* 3 (2023), 300013.
- [35] Z. Xin, Z. Yuan, J. Liu, X. Wang, K. Shen, Y. Chen, Y.-Q. Lan, Cu cluster embedded porous nanofibers for high-performance CO<sub>2</sub> electroreduction, *Chin. Chem. Lett.* 34 (2023).
- [36] Z.H. Zhu, B.H. Zhao, S.L. Hou, X.L. Jiang, Z.L. Liang, B. Zhang, B. Zhao, A facile strategy for constructing a carbon-particle-modified metal-organic framework for enhancing the efficiency of CO<sub>2</sub> electroreduction into formate, *Angew. Chem. Int. Ed.* 60 (2021) 23394–23402.
- [37] C. Ye, M. Zheng, Z. Li, Q. Fan, H. Ma, X. Fu, D. Wang, J. Wang, Y. Li, Electrical pulse induced one-step formation of atomically dispersed Pt on oxide clusters for ultra-low-temperature zinc-air battery, *Angew. Chem. Int. Ed.* 61 (2022), e202213366.
- [38] B.-B. Xu, X.-B. Fu, X.-M. You, E. Zhao, F.-F. Li, Z. Chen, Y.-X. Li, X.L. Wang, Y.-F. Yao, Synergistic promotion of single-atom Co surrounding a PtCo alloy based on a g-C<sub>3</sub>N<sub>4</sub> nanosheet for overall water splitting, *ACS Catal.* 12 (2022) 6958–6967.
- [39] L. Hui, X. Zhang, Y. Xue, X. Chen, Y. Fang, C. Xing, Y. Liu, X. Zheng, Y. Du, C. Zhang, F. He, Y. Li, Highly dispersed platinum chlorine atoms anchored on gold quantum dots for a highly efficient electrocatalyst, *J. Am. Chem. Soc.* 144 (2022) 1921–1928.
- [40] X. Li, X.I. Pereira-Hernandez, Y. Chen, J. Xu, J. Zhao, C.W. Pao, C.Y. Fang, J. Zeng, Y. Wang, B.C. Gates, J. Liu, Functional CeO<sub>x</sub> nanogels for robust atomically dispersed catalysts, *Nature* 611 (2022) 284–288.
- [41] X. Liu, K. Zhang, Y. Sun, S. Zhang, Z. Qiu, T. Song, J. Xie, Y. Wu, Y. Chen, Upgrading CO<sub>2</sub> into acetate on Bi<sub>2</sub>O<sub>3</sub>@carbon felt integrated electrode via coupling electrocatalysis with microbial synthesis, *SusMat* 3 (2023) 235–247.
- [42] J. Hafner, Ab-initio simulations of materials using VASP: density-functional theory and beyond, *J. Comput. Chem.* 29 (2008) 2044–2078.
- [43] P.E. Blöchl, Projector augmented-wave method, *Phys. Rev. B* 50 (1994) 17953.
- [44] J.P. Perdew, K. Burke, M. Ernzerhof, Generalized gradient approximation made simple, *Phys. Rev. Lett.* 77 (1996) 3865.
- [45] S. Grimme, Semiempirical GGA-type density functional constructed with a long-range dispersion correction, *J. Comput. Chem.* 27 (2006) 1787.
- [46] H.J. Monkhorst, J.D. Pack, Special points for Brillouin-zone integrations, *Phys. Rev. B* 13 (1976) 5188.
- [47] V. Wang, N. Xu, J.-C. Liu, G. Tang, W.-T. Geng, VASPKIT: a user-friendly interface facilitating high-throughput computing and analysis using VASP code, *Comput. Phys. Commun.* 267 (2021), 108033.
- [48] S. Reinoso, P. Vitoria, L. Lezama, A. Luque, J.M. Gutiérrez-Zorrilla, A novel organic-inorganic hybrid based on a dinuclear copper complex supported on a Keggin polyoxometalate, *Inorg. Chem.* 42 (2003) 3709–3711.
- [49] P. Xie, J. Ding, Z. Yao, T. Pu, P. Zhang, Z. Huang, C. Wang, J. Zhang, N. Zecher-Freeman, H. Zong, D. Yuan, S. Deng, R. Shahbazian-Yassar, C. Wang, Oxo dicopper anchored on carbon nitride for selective oxidation of methane, *Nat. Commun.* 13 (2022) 1375.

- [50] T.P. Gerasimova, S.A. Katsyuba, Bipyridine and phenanthroline IR-spectral bands as indicators of metal spin state in hexacoordinated complexes of Fe(ii), Ni(ii) and Co(ii), *Dalton Trans.* 42 (2013) 1787–1797.
- [51] X. An, Q. Tang, H. Lan, H. Liu, X. Yu, J. Qu, H. Lin, J. Ye, Facilitating molecular activation and proton feeding by dual active sites on polymeric carbon nitride for efficient CO<sub>2</sub> photoreduction, *Angew. Chem. Int. Ed.* 61 (2022), e202212706.
- [52] Y. Zhu, K. Fan, C.S. Hsu, G. Chen, C. Chen, T. Liu, Z. Lin, S. She, L. Li, H. Zhou, Y. Zhu, H.M. Chen, H. Huang, Supported ruthenium single-atom and clustered catalysts outperform benchmark Pt for alkaline hydrogen evolution, *Adv. Mater.* (2023), e2301133.
- [53] G. Chen, Y. Zhu, H.M. Chen, Z. Hu, S.F. Hung, N. Ma, J. Dai, H.J. Lin, C.T. Chen, W. Zhou, Z. Shao, An amorphous nickel-iron-based electrocatalyst with unusual local structures for ultrafast oxygen evolution reaction, *Adv. Mater.* 31 (2019), e1900883.
- [54] Y. Zhu, G. Chen, Y. Zhong, Y. Chen, N. Ma, W. Zhou, Z. Shao, A surface-modified antiperovskite as an electrocatalyst for water oxidation, *Nat. Commun.* 9 (2018) 2326.
- [55] G.P. Mane, S.N. Talapaneni, K.S. Lakhi, H. Ilbeygi, U. Ravon, K. Al-Bahily, T. Mori, D.H. Park, A. Vinu, Highly ordered nitrogen-rich mesoporous carbon nitrides and their superior performance for sensing and photocatalytic hydrogen generation, *Angew. Chem. Int. Ed.* 56 (2017) 8481–8485.
- [56] Z. Chen, S. Mitchell, E. Vorobyeva, R.K. Leary, R. Hauert, T. Furnival, Q. M. Ramasse, J.M. Thomas, P.A. Midgley, D. Dontsova, M. Antonietti, S. Pogodin, N. López, J. Pérez-Ramírez, Stabilization of single metal atoms on graphitic carbon nitride, *Adv. Funct. Mater.* 27 (2017).
- [57] Y. Yang, C.L. Wang, S.Q. Gao, K.T. Mao, G.L. Xia, Z.Y. Lin, P. Jiang, L. Hu, Q. W. Chen, Incorporation of Cu-N-x cofactors into graphene encapsulated Co as biomimetic electrocatalysts for efficient oxygen reduction, *Nanoscale* 10 (2018) 21076–21086.
- [58] X. Yang, J. Cheng, B.Z. Fang, X.X. Xuan, N. Liu, X. Yang, J.H. Zhou, Single Ni atoms with higher positive charges induced by hydroxyls for electrocatalytic CO<sub>2</sub> reduction, *Nanoscale* 12 (2020) 18437–18445.
- [59] C. Zhu, L. Lu, Q. Fang, S. Song, B. Chen, Y. Shen, Unveiling spin state-dependent micropollutant removal using single-atom covalent triazine framework, *Adv. Funct. Mater.* 33 (2023), 202210905.
- [60] Y. Shen, J. Yang, C. Zhu, Q. Fang, S. Song, B. Chen, Mechanistic insights into the atomic distance effect on adsorption and degradation of aromatic compounds, *ACS Catal.* 13 (2023) 8943–8954.
- [61] J. Xu, C. Zhu, S. Song, Q. Fang, Y. Shen, A nanocubicle-like 3D adsorbent fabricated by in situ growth of 2D heterostructures for removal of aromatic contaminants in water, *J. Hazard. Mater.* 423 (2022), 127004.
- [62] Y. Shen, J. Wu, C. Zhu, J. Zhao, Q. Fang, Y. Zheng, C.T.J. Ferguson, S. Song, Bifunctional covalent triazine frameworks based on Ti-ON bonds for micropollutants removal: effects of 3D extended structure and electron transport bridges, *Chem. Eng. J.* 465 (2023), 143026.
- [63] Q.X. Lai, J.J. Zhu, Y.X. Zhao, Y.Y. Liang, J.P. He, J.H. Chen, MOF-based metal-doping-induced synthesis of hierarchical porous Cu-N/C oxygen reduction electrocatalysts for Zn-air batteries, *Small* 13 (2017) 11.
- [64] L. Liu, A. Corma, Metal catalysts for heterogeneous catalysis: from single atoms to nanoclusters and nanoparticles, *Chem. Rev.* 118 (2018) 4981–5079.
- [65] Z.S. Chen, G.X. Zhang, L. Du, Y. Zheng, L.X. Sun, S.H. Sun, Nanostructured cobalt-based electrocatalysts for CO<sub>2</sub> reduction: recent progress, challenges, and perspectives, *Small* 16 (2020) 32.
- [66] S. Chen, X. Li, C.W. Kao, T. Luo, K. Chen, J. Fu, C. Ma, H. Li, M. Li, T.S. Chan, M. Liu, Unveiling the proton-feeding effect in sulfur-doped Fe-N-C single-atom catalyst for enhanced CO<sub>2</sub> electroreduction, *Angew. Chem. Int. Ed. Engl.* 61 (2022), e202206233.
- [67] Y. Shen, H. Zhang, B. Chen, C. Zhu, W. Yu, J. Yang, Q. Fang, Z. He, T. Sun, S. Song, Mechanistic insight into electron orientation by tailoring Ni-Cu atom-pairs for high-performance CO<sub>2</sub> electroreduction, *Appl. Catal. B Environ.* 330 (2023), 122654.
- [68] D. Ren, B.S.-H. Ang, B.S. Yeo, Tuning the selectivity of carbon dioxide electroreduction toward ethanol on oxide-derived Cu<sub>x</sub>Zn catalysts, *ACS Catal.* 6 (2016) 8239–8247.
- [69] C. Zhan, F. Dattila, C. Rettenmaier, A. Bergmann, S. Kuhl, R. Garcia-Muelas, N. Lopez, B.R. Cuenya, Revealing the CO coverage-driven C-C coupling mechanism for electrochemical CO<sub>2</sub> reduction on Cu<sub>2</sub>O nanocubes via Operando Raman spectroscopy, *ACS Catal.* 11 (2021) 7694–7701.
- [70] Y. Mao, J. He, X. Sun, W. Li, X. Lu, J. Gan, Z. Liu, L. Gong, J. Chen, P. Liu, Y. Tong, Electrochemical synthesis of hierarchical Cu<sub>2</sub>O stars with enhanced photoelectrochemical properties, *Electrochim. Acta* 62 (2012) 1–7.
- [71] X. Yan, M. Zhang, Y. Chen, Y. Wu, R. Wu, Q. Wan, C. Liu, T. Zheng, R. Feng, J. Zhang, C. Chen, C. Xia, Q. Zhu, X. Sun, Q. Qian, B. Han, Synergy of Cu/C<sub>3</sub>N<sub>4</sub> interface and Cu nanoparticles dual catalytic regions in electrolysis of CO to acetic acid, *Angew. Chem. Int. Ed.* 62 (2023), e202301507.
- [72] H. An, L. Wu, L.D.B. Mandemaker, S. Yang, J. de Ruiter, J.H.J. Wijten, J.C. L. Janssens, T. Hartman, W. van der Stam, B.M. Weckhuysen, Sub-second time-resolved surface-enhanced Raman spectroscopy reveals dynamic CO intermediates during electrochemical CO<sub>2</sub> reduction on copper, *Angew. Chem. Int. Ed.* 60 (2021) 16576–16584.